Defects, dopants and lithium incorporation in LiPON electrolyte

Kuganathan, K. & Chroneos, A.

Original citation & hyperlink:
Kuganathan, K & Chroneos, A 2022, 'Defects, dopants and lithium incorporation in LiPON electrolyte', Computational Materials Science, vol. 202, 111000.
https://dx.doi.org/10.1016/j.commatsci.2021.111000

DOI 10.1016/j.commatsci.2021.111000
ISSN 0927-0256

Publisher: Elsevier

Defects, Dopants and Lithium incorporation in LiPON electrolyte

Navaratnarajah Kuganathan[1,2*] and Alexander Chroneos[1,2,3]

[1]Department of Materials, Imperial College London, London, SW7 2AZ, United Kingdom

[2]Faculty of Engineering, Environment and Computing, Coventry University, Priory Street, Coventry CV15FB, United Kingdom

[3]Department of Electrical and Computer Engineering, University of Thessaly, 38221 Volos, Greece

---

Abstract

Lithium phosphorus oxy-nitride (LiPON) is a candidate solid electrolyte material for potential use in rechargeable lithium-ion batteries. The use of density functional theory simulations has allowed us to gain atomic-scale insight into the defect properties, solution of dopants and incorporation of lithium in LiPON. The Li_2O Schottky is the most favourable disorder process in this material ensuring the formation of Li and O vacancies which are in turn required for vacancy mediated self-diffusion. The Na, As and S are the promising isovalent dopants that can be substituted on the Li, P and O sites respectively. The doping of Mg on the Li site leads to the formation of Li vacancies in LiPON. The promising dopant on the P site to create Li interstitials and oxygen vacancies is the Ge. The stability of the crystal structure upon Li incorporation (up to four Li) was considered. The incorporation confirmed the formation of Li^+ ions and expanded the volume of the lattice. Incorporation of multiple Li atoms is more favourable than a single Li incorporation. The band gap of this material decreases upon of Li incorporation without changing its insulating character.

Keywords: Defects; dopants; LiPON; DFT; incorporation

*Corresponding author, e-mail: n.kuganathan@imperial.ac.uk

1. Introduction

Lithium-ion batteries (LIBs) are attracting growing interest for numerous applications including portable electronics, electric vehicles and grid storage systems due to high energy density, safety and lightweight [1-4]. LIBs provide a method of converting chemical energy into electrical energy efficiently and reduce CO_2 emission mainly arising from fossil fuel based transportation. The capacity of battery electricity is dependent on promising electrode and electrolyte materials.

Properties of electrolytes play a key role in the performance of LIBs. Much attention has been paid to solid electrolytes as there is a practical difficulty of fabricating microscale batteries using liquid electrolytes [5-8]. A variety of solid electrolyte materials with high Li-ion conductivities including $Li_{10}GeP_2S_{12}$ [9], $Li_7P_3S_{11}$ [10] and $Li_{1.3}Al_{0.3}Ti_{1.7}(PO_4)_3$ [11], $LiBH_4$ [12], $Li_{9.54}Si_{1.74}P_{1.44}S_{11.7}Cl_{0.3}$ [13] and Li_3ClO [14] have been assessed. Garnet-type $Li_7La_3Zr_2O_{12}$ (LLZO) solid electrolyte [15] was recently proposed as a promising solid electrolyte for all-solid-state LIBs as it exhibited high Li-ion conductivity and a wide electrochemical stability window.

LiPON (Li_2PO_2N) is a material that was considered as a potential electrolyte material in its amorphous form in thin-film rechargeable Li-ion batteries thirty years ago due to its promising ionic conductivity with an activation energy of 0.55 eV, good cyclic performance, high electronic resistivity and large electrochemical window [16-20]. Good electrochemical performance and high Li-ion conductivity are commonly linked to the presence of N in this material [21]. Incorporation of N has significantly increased the Li-ion conduction and reduced the activation energy in an experimental study carried out by Bates *et al.* [22]. Several experimental techniques were applied to synthesize this material in its crystalline form. However, only a few of them were successfully achieved to produce stable LiPON crystalline phase with high ionic conductivity. Senevirathne *et al.* [17] used a stoichiometric mixture of Li_2O, P_2O_5 and P_3N_5 at high temperature to prepare crystalline LiPON. This compound was stable in air up to 600° C and had an activation energy of 0.60 eV according to electrochemical spectroscopy measurements [17]. Density functional theory (DFT) simulations performed by the same authors shows that vacancy and interstitial assisted Li-ion migration energies are calculated to be 0.40 eV and 0.80 eV respectively [17]. Furthermore, the insulating nature of this material was identified with a band gap of larger than 6 eV. Lacivita *et al.* [21] performed molecular dynamics (MD) simulations to generate models of LiPON and examined the Li-ion diffusion in the presence of Li and N substitution. A stable interface layer formed between LiPON and metallic Li was studied using X-ray photoemission spectroscopy and its chemical reactivity was examined [19]. Chemical reactions at the interface led to the decomposition products such as Li_3PO_4, Li_3P, Li_3N and Li_2O. In the experimental study by Put *et al.* [20], the decomposition of LiPON layer was observed at a potential of 4.3 V forming decomposition products such as Li^+ ions, O_2 or N_2 gas and a phosphate rich compound. Although there are reasonable amount of experimental work carried out in this material, only a few theoretical studies [21,23,24] have been reported. In particular, intrinsic defects and subsitutional doping in an electrolyte material have a major impact on battery performance. To the best of our knowledge, no studies have

been reported on defects and dopants in LiPON.

In this study, spin-polarised DFT simulation together with dispersion corrections was employed to examine the intrinsic defect properties, solution of dopants, Li incorporation and reaction energetics for the formation of LiPON using different synthetic routes.

2. Computational Methods

All calculations were performed using DFT with spin polarization as implemented in the VASP package [25]. The exchange-correlation term was formulated using the generalized gradient approximation (GGA) as described by Perdew, Burke, and Ernzerhof (PBE) [26]. A plane-wave basis set with a cut off value of 500 eV and standard projected augmented wave (PAW) potentials were used [27]. The valence electronic configurations of Li, N, O, and P were $2s^1$, $2s^22p^3$ $2s^22p^4$ and $3s^23p^3$ respectively. A 1 × 2× 2 supercell containing 96 atoms was used for the defect calculations. A 4×4×4 Monkhorst-Pack [28] *k* point mesh, which yielded 36 k points was used in all calculations. Conjugate gradient algorithm [29] was used to optimize both bulk and defect structures. The forces on the atoms in all optimized structures were smaller than 0.001 eV/Å. In this work, van der Waals (vdW) interactions were included in the form of semi-empirical pair-wise force field as implemented by Grimme *et al.* [30] in the VASP package.

3. Results and discussion

3.1. Crystal structre of LiPON

The crystal structure of LiPON is orthorhombic and belongs to the space group $Cmc2_1$ (no: 36) with unit cell parameters a = 9.0692, b = 5.3999, c = 4.6856 Å and α=β=γ=90° [17]. The structure consists of chains of corner sharing LiO_3N and PO_2N_2 tetrahedral units in the *ab* plane (see Figure 1a). Full geometry optimization was carried out to obtain equilibrium lattice parameters to validate the choice of the basis sets and pseudopotentials. Calculated lattice parameters together with experimental values are reported in Table 1. There is a good agreement between the calculated and experimental values. The total density of states (DOS) plots is shown in Figure 1b. The bulk LiPON exhibits an insulating behaviour with a band gap of 6.40 eV in agreement with the value (6.00 eV) calculated in a previous DFT study performed by Senevirathne *et al.*[17]. The Bader charge analysis [31] shows the full ionic nature of Li, P, N and O (see Table 2).

3.2. Formation energetics of LiPON

Here, we calculate formation energies of LiPON that can be synthesised using different chemical reactions as shown below.

$$Li_2O + \frac{1}{5}P_2O_5 + \frac{1}{5}P_3N_5 \rightarrow Li_2PO_2N \quad (1)$$

$$2\,Li + \frac{1}{4}P_4 + O_2 + \frac{1}{2}N_2 \rightarrow Li_2PO_2N \quad (2)$$

$$2\,Li + \frac{1}{4}P_4 + NO_2 \rightarrow Li_2PO_2N \quad (3)$$

$$\frac{1}{2}Li_4P_2O_7 + NO \rightarrow Li_2PO_2N + \frac{5}{4}O_2 \quad (4)$$

$$Li_2O + \frac{1}{2}P_2O_5 + \frac{1}{2}N_2 \rightarrow Li_2PO_2N + \frac{3}{4}O_2 \quad (5)$$

$$Li_3N + LiPO_3 \rightarrow Li_2PO_2N + Li_2O \quad (6)$$

Reaction energy was calculated for reaction 1 using the following equation. Similar equations were used for the other reactions.

$$E_R = E(Li_2PO_2N) - E(Li_2O) - \frac{1}{5}E(P_2O_5) - \frac{1}{5}E(P_3N_5) \quad (7)$$

where $E(Li_2PO_2N), E(Li_2O), E(P_2O_5)$ and $E(P_3N_5)$ are total energies of Li_2PO_2N, Li_2O, P_2O_5 and P_3N_5 respectively.

In Table 3, we report formation energy and atom economy for each chemical reactions. Reaction 1 was used to synthesise crystalline LiPON by Senevirathne *et al.* [17]. Formation energy for this reaction is −2.66 eV meaning that this process is thermodynamically feasible. Atom economy for this process is 100 % (atomic economy = $\frac{mass\ of\ desired\ product}{mass\ of\ total\ reactants} \times 100\ \%$). In reaction 2, constituent elements in their standard states are used to produce one mole of LiPON. This process is highly exothermic (−12.22 eV) with an atom economy of 100%. In the third reaction, reactants N_2 and O_2 are replaced by NO_2. This reaction is slightly endothermic (by ~ 0.20 eV) than the reaction 2. In reaction 4, solid $Li_4P_2O_7$ and NO gas were allowed to react together to form LiPON. This reaction has a formation energy of 2.59 eV and yields oxygen as a side product. Atom economy for this reaction is 69.5 % and this lower value is due to the formation of side product. Reverse reaction of this process is the oxidation of LiPON with the reaction energy of −2.59 eV. This indicates that LiPON is unstable under air. In the reaction 5, Li_2O and P_2O_5 together with N_2 were used to form the same products as in the reaction 4. This reaction is endothermic and thermodynamically unfavourable. In the last reaction (equation 6), Li_3N and $LiPO_3$ were considered as reactants as outlined in an experimental study [32] in which microcrystalline $Li_{2.88}PO_{3.77}N_{0.17}$ was prepared using those reactants under the atmosphere of N_2 at low temperature. In our simulation study, the products are Li_2PO_2N and Li_2O and this process is exothermic (−4.22 eV) indicating that this experimental route is also thermodynamically favourable.

3.3. Defect properties

The presence of point defects in a material influences its properties. Point defect energies were first calculated and then they were combined together with appropriate lattice energies to calculate Frenkel and Schottky defect processes. Anti-site defects in which cations or anions swap their positions were also considered. This defect has dominated many oxide materials enhancing or degrading their chemical and physical properties [33-35]. The following reaction equations were used to describe the intrinsic defect processes in LiPON using the Kröger–Vink notation [36]. The lattice parameters calculated for bulk Li_2O and P_2O_5 structures together with experimental values are provided in the electronic supplementary information (ESI) (see Table S1).

Li Frenkel: $Li_{Li}^{X} \rightarrow V_{Li}' + Li_i^{\bullet}$ (8)

P Frenkel: $P_P^{X} \rightarrow V_P'''' + P_i^{\bullet\bullet\bullet\bullet\bullet}$ (9)

N Frenkel: $N_N^{X} \rightarrow V_N^{\bullet\bullet\bullet} + N_i'''$ (10)

O Frenkel: $O_O^X \rightarrow V_O^{\bullet\bullet} + O_i''$ (11)

Schottky: $2\,Li_{Li}^X + P_P^X + N_N^X + 2\,O_O^X \rightarrow 2\,V_{Li}' + V_P''''' + V_N^{\bullet\bullet\bullet} + 2\,V_O^{\bullet\bullet} + Li_2PO_2N$ (12)

Li_2O Schottky: $2\,Li_{Li}^X + O_O^X \rightarrow 2\,V_{Li}' + V_O^{\bullet\bullet} + Li_2O$ (13)

P_2O_5 Schottky: $2\,P_P^X + 5\,O_O^X \rightarrow 2\,V_P''''' + 5\,V_O^{\bullet\bullet} + P_2O_5$ (14)

Li/P anti–site (isolated): $Li_{Li}^X + P_P^X \rightarrow Li_P'''' + P_{Li}^{\bullet\bullet\bullet\bullet}$ (15)

Li/P anti–site (cluster): $Li_{Li}^X + P_P^X \rightarrow \{Li_P'''' + P_{Li}^{\bullet\bullet\bullet\bullet}\}^X$ (16)

Formation energy of Li Frenkel pair (FP_{Li}) was calculated combining the formation energies of Li vacancy and Li interstitial, that is:

$$E_{for}(FP_{Li}) = E_{for}(V_{Li}') + E_{for}(Li_i^{\bullet}) \quad (17)$$

In order to calculate the formation energies for Schottky and anti-site defects, the following equations were used.

$$E_{for}(\text{Schottky}) = 2\,E\,[V_{Li}']_{1\times2\times2} + E\,[V_P''''']_{1\times2\times2} + E\,[V_N^{\bullet\bullet\bullet\bullet\bullet}]_{1\times2\times2} + 2\,E\,[V_O^{\bullet\bullet}]_{1\times2\times2} - 6\times\frac{95}{96}E[\text{LiPON}]_{1\times2\times2} \quad (18)$$

$$E_{for}(Li_2O\ \text{Schottky}) = 2\,E\,[V_{Li}']_{1\times2\times2} + E\,[V_O^{\bullet\bullet}]_{1\times2\times2} + E(Li_2O) - 3\times\frac{95}{96}E[\text{LiPON}]_{1\times2\times2} \quad (19)$$

$$E_{for}(P_2O_5\ \text{Schottky}) = 2\,E\,[V_P''''']_{1\times2\times2} + 5\,E\,[V_O^{\bullet\bullet}]_{1\times2\times2} + E(P_2O_5) - 7\times\frac{95}{96}E[\text{LiPON}]_{1\times2\times2} \quad (20)$$

$$E_{for}(\text{Li/P anti}-\text{site})(\text{isolated}) = E\,[Li_P'''']_{1\times2\times2} + E\,[P_{Li}^{\bullet\bullet\bullet\bullet}]_{1\times2\times2} - 2\times\frac{95}{96}E[\text{LiPON}]_{1\times2\times2} \quad (21)$$

where $E\,[V_{Li}']_{1\times2\times2}$, $E\,[V_P''''']_{1\times2\times2}$, $E\,[V_N^{\bullet\bullet\bullet\bullet\bullet}]_{1\times2\times2}$, $E\,[V_O^{\bullet\bullet}]_{1\times2\times2}$ are the total energies of a 1×2×2 supercell consisting of a single Li, P, N and O vacancy respectively. $E\,[Li_P'''']_{1\times2\times2}$ and $E\,[P_{Li}^{\bullet\bullet\bullet\bullet}]_{1\times2\times2}$ are the total energies of a 1×2×2 supercell consisting of Li_P'''' and $P_{Li}^{\bullet\bullet\bullet\bullet}$ defects respectively. $E(Li_2O)$ and $E(P_2O_5)$ are the total energies Li_2O and P_2O_5 per formula unit respectively. Table 4 lists the intrinsic defect process energies. The Li_2O Schottky is the most favourable intrinsic defect process. This process can facilitate the loss of Li_2O and degrade the crystal structure. A high temperature is required as this process is endoergic with a defect energy of 2.27 eV. In a previous simulation study, we have shown that the Li_2O Schottky is a dominant disorder process in cubic LLZO electrolyte material [37]. The loss of Li_2O was observed experimentally in related materials such as Li_5FeO_4 and this process led to the extraction of lithium in this material assisted by the release of oxygen [38]. The second most favourable defect process is the Schottky which is higher by 0.71 eV than the Li_2O Schottky. The O Frenkel is the third most favourable defect. Both Li Frenkel and N Frenkel have a defect energy of ~4 eV indicating that the concentration of Li and N vacancies is not significant in this material at room temperature. Other Schottky and Frenkel defect processes are highly exothermic. In particular, P Frenkel has a defect energy of 10.03 eV and this process is highly unfavourable. The Li-P anti-site defect was also calculated in the form of isolated and cluster. While

Li_P''' and $P_{Li}^{\bullet\bullet\bullet\bullet}$ defects were calculated separately in the isolated form, both defects were considered closer to each other in the cluster form and their energies calculated. The Li-P cluster anti-site defect energy is favourable than its isolated form. This is due to the aggregation of isolated defects forming cluster with a negative binding energy of −1.83 eV. Nevertheless, defect energies are highly exothermic for both isolated and cluster forms. This is partly due to high charge mismatch between P^{5+} and Li^{+} ions.

3.4. Solution of dopants

The functional properties of a material strongly depend on the concentration of point defects. With appropriate aliovalent dopants, the concentration of point defects can be increased. Here, we considered a variety of isovalent and aliovalent dopants at different sites and calculated the solution energies. The solution energy for a particular dopant provides an indication of how easily the dopant ion can be substituted. Appropriate lattice energies for different oxides were calculated and used to calculate solution energies. The results on the doping from this simulation study can be used to tune LiPON as a promising electrolyte material.

In the ESI, we provide the calculated lattice parameters of different bulk structures used in this section together with their experimental values [see Table S1].

3.4.1. Alkali dopants

First we considered alkali dopants (M = Na, K, Rb and Cs) on the Li site. The reaction equation for this process is as follows.

$$\frac{1}{2}M_2O + Li_{Li}^{X} \rightarrow M_{Li}^{X} + \frac{1}{2}Li_2O \quad (22)$$

The following equation was used to calculate the solution energy.

$$E_{Sol} = E\,[M_{Li}^{X}]_{1\times2\times2} + \frac{1}{2}E\,[Li_2O] - \frac{1}{2}E\,[M_2O] - E[LiPON]_{1\times2\times2} \quad (23)$$

where $E\,[M_{Li}^{X}]_{1\times2\times2}$ is the total energy of a LiPON supercell consisting of M_{Li}^{X} defect, $E[LiPON]_{1\times2\times2}$ is the total energy of a LiPON supercell and $E\,[M_2O]$ is the total energy per formula unit of a dopant oxide.

The most favourable dopant for this process is the Na and its solution energy is calculated to be −0.04 eV (see Table 5). As this is an exothermic reaction, it possible to synthesis $Li_{1-x}Na_xPO_2N$ experimentally. The preference of Na can be due to the ionic radius of Li^{+} (0.76 Å) [**39**] which is closer to the ionic radius of Na^{+} (0.99 Å) [**39**]. Endothermic solution energies are calculated for the other dopants. Solution energy increases with the increasing ionic radius and volume. The highest solution energy dopant is the Cs with the solution energy of 6.02 eV indicating that this dopant cannot be substituted under normal conditions.

Tetrahedral units consisting of dopants and the nearest neighbour oxygen in the relaxed structures are shown in Figure 2. In the optimised LiPON crystal structure, Li-O bond distances and bond angles are 1.56–1.63 Å and 108.4 –111.0° respectively. In the NaO_4 unit, all four Na-O bond distances (2.12–2.24 Å) and bond angles (104.3–122.2°) are significantly larger than that found in the LiO_4 unit. This is partly due to the larger ionic radius of Na^{+} than that of Li^{+}. Elongation in the

bond length and bond angles increases with increasing ionic radius of the dopants. The higher positive solution energy is partly associated with the larger elongation in the tetrahedral unit. The total DOS plots calculated for the doped-LiPON structures show that there is a small increase in the Fermi energy. The top of the valence band shift towards conduction band with increasing ionic radius of the dopants. The bottom of the conduction band shift slightly towards valence band maximum. Due to the shifts of those two bands, there is a slight reduction in the band gap, but the resultant doped structures are still insulator. Atomic DOS plots show that the edges of the valence and conduction bands mainly consisted of states belongs to the dopants.

3.4.2. Alkali earth dopants

Next, alkali-earth dopants (Mg, Ca, Sr and Ba) were considered on the Li site to introduce Li vacancies in the lattice according to the following equation.

$$MO + 2\,Li_{Li} \rightarrow M_{Li}^{\bullet} + V_{Li}' + Li_2O \quad (24)$$

Solution energy was calculated using the following equation.

$$E_{Sol} = E\,[M_{Li}^{\bullet} + V_{Li}']_{1\times2\times2} + E\,[Li_2O] - E\,[MO] - E[LiPON]_{1\times2\times2} \quad (25)$$

where $E\,[M_{Li}^{\bullet} + V_{Li}']_{1\times2\times2}$ is the total energy of a supercell containing $M_{Li}^{\bullet}$ and V_{Li}' defects.

Here, we considered the defects ($M_{Li}^{\bullet}$ and V_{Li}') further apart and next to each other (cluster) in the lattice. Solution energy calculated for the cluster form is more favourable than that calculated for the defects present further away. This is due to the aggregation of defects forming a cluster with negative binding energy. The lowest solution energy (2.08 eV) is calculated for Mg (see Table 6). This is because the ionic radius of Mg^{2+} (0.71 Å)[***39***] closer to that of Li^{+}. Solution energy increases with increasing ionic radius and binding energy. The distortion of the lattice also increases as evidenced by the expansion of volume (see Table 6) and elongation in the dopant-oxygen bond lengths and bond angles (see Figure 3).

A small increase in the Fermi energy compared to defect free LiPON is observed for all dopant substitution. The dopant Ba which has the largest ionic radius exhibits the lowest Fermi energy. There are no states present in the band gap for all dopants. For Mg, the *s* and *p* states appear in the valence band region of 0–3 eV. For the other dopants, these states should be present in the deeper level of the valence band. In all cases, the band gap is ~5.60 eV which is smaller by 0.80 eV than the value calculated for the pristine LiPON. Overall, the insulating nature is unaffected by the doping.

3.4.3. Tetravalent dopants

The capacity of LiPON can be increased by creating extra Li^{+} ions. Doping of tetravalent cations (Si, Ge, Ti, Sn, Zr and Ce) was considered on the P site. Additional Li^{+} ions in the form of Li interstitials are produced in this process according to the following reaction equation.

$$\tfrac{1}{2}Li_2O + MO_2 + P_P^X \rightarrow M_P' + Li_i^{\bullet} + \tfrac{1}{2}\,P_2O_5 \quad (26)$$

$$E_{Sol} = E\,[M_P' + Li_i^{\bullet}]_{1\times2\times2} + \tfrac{1}{2}E\,[P_2O_5] - \tfrac{1}{2}E\,[Li_2O] - E\,[MO_2] - E[LiPON]_{1\times2\times2}$$

where $E\,[M_P' + Li_i^{\bullet}]_{1\times2\times2}$ is the total energy of a supercell containing M_P' and $Li_i^{\bullet}$ defects and $E\,[P_2O_5]$

is the total energy of per formula unit of bulk P_2O_5.

The most favourable dopant for this process is the Ge with the solution energy of 1.52 eV (see Table 7). The cluster form in which both M_P' and $Li_i^{\bullet}$ defects are closer to each other is more favourable than the isolated form. In the isolated form, defects are present further apart. As discussed earlier, the formation of defect cluster is facilitated by the exoergic binding of defects. The second most favourable dopant is the Si. In general, solution energy increases with increasing ionic radius except for Ge. The solution energy calcualted for the Ce is highly endothermic and this dopant requires high temperture.

Relaxed tetrahedral units consisting of dopants are shown in Figure 4. In general, there is a distrotion upon doping and this distortion increases with increasing ionic radius. This is further evidenced by the expansion of volume (see Table 7). Total DOS plots calculated for doped configurations and atomic DOS plots calculated for dopnts are shown in Figure 5. Fermi energy has slightly increased with the introduction of dopants. A significant increment is noted for Ce. Doping introduced gap states belong to the dopants and reduced the bandgap of LiPON. Nevertheless, the material is still an insulator.

The tetravalent doping on the P site can also introduce oxygen vacancies as charge compensating defects as explained in the following reaction equation.

$$2\,MO_2 + 2\,P_P^X + O_O^X \rightarrow 2\,M_P' + V_O^{\bullet\bullet} + P_2O_5 \quad (27)$$

$$E_{Sol} = E\,[2M_P' + V_O^{\bullet\bullet}]_{1\times2\times2} + E\,[P_2O_5] - 2\,E\,[MO_2] - E[LiPON]_{1\times2\times2} \quad (28)$$

where $E\,[2M_P' + V_O^{\bullet\bullet}]_{1\times2\times2}$ is the total energy of supercell consisting of two M_P' and $V_O^{\bullet\bullet}$ defects.

The cluster form $\{2\,M_P' : V_O^{\bullet\bullet}\}$ exhibited lower solution energy than its isolated form in all cases (see Table 7). The solution energy calculated for oxygen vacancy formation is slighly higher than that calculated for Li interstitial. The dopant Ge is the promising dopant, although its solution energy is endothermic (2.22 eV). Solution energy calculated for the Si is higher by 1.70 eV than that calculated for the Ge. Other dopants exhibit even more higher solution energies. The highest solution energy calculated for Ce indicates that this dopant is unfavourable under normal conditions.

Structural parameters (i.e. bond lenghts and bond angles) in the relaxed MO_2N_2 tetrahedral units are shown in Figure 6. There is a gradual expansion in the bond lengths and bond angles with increasing ionic radius. The Fermi energy for Si-doped configuration is slightly higher than that calculated for defect free LiPON. For dopants Ge and Ti, Fermi energy is slightly lowered. For the dopant Sn, Fermi energy has increased. A significant increase is observed for Ce. In all cases, there is a slight reduction in the band gap (see Figure 7). The states appear in the band gap are associated with the dopants. The doped configurations exhibit insulating character as observed for pristine LiPON.

3.4.4. Pnictogen dopants

Next, pnictogen dopants (M = As, Sb and Bi) were substituted on the P site and the solution energies were calculated using the following equation.

$$\frac{1}{2}M_2O_5 + P_P^X \rightarrow M_P^X + \frac{1}{2}P_2O_5 \quad (29)$$

We used the following equation to calculate solution energies.

$$E_{Sol} = E\,[M_P^X]_{1\times2\times2} + \frac{1}{2}E\,[P_2O_5] - \frac{1}{2}E\,[M_2O_5] - E[LiPON]_{1\times2\times2} \quad (30)$$

where $E\,[M_P^X]_{1\times2\times2}$ is the total energy of a supercell consisting of M_P^X defect.

Solution energies and volume changes are reported in Table 8. The dopant As has the lowest solution energy of 0.60 eV. This is partly due to the ionic radius of P (0.29 Å)[**39**] closer to that of As (0.34 Å)[**39**]. Dopant with larger ionic radius results in higher solution energy. Solution energy calculated for Bi is relatively very high meaning that this dopant is impossible to substitute at any condition. There is a small expansion of volume upon doping of As and expansion increases with the ionic radius of the dopant ion. In Figure 8, optimised tetrahedral units having dopants and DOS plots are shown. As dopant size increases both bond lengths and bond angles also increase. The Fermi energy level does not alter significantly upon doping. The *s* states of dopants appear in the band gap. There is only a slight reduction in the band gap in all cases without altering overall electronic nature.

3.4.5. Chalcogen dopants

Chalcogen dopants (M = S, Se and Te) on the O site were also considered. Solution energies were calculated using appropriate lattice energies. The reference states used for S, Se and Te are bulk S_8, bulk Se and bulk Te respectively (see equations 31-33).

$$\frac{1}{8}S_8 + O_O^X \rightarrow S_O^X + \frac{1}{2}O_2 \quad (31)$$

$$Se + O_O^X \rightarrow Se_O^X + \frac{1}{2}O_2 \quad (32)$$

$$Te + O_O^X \rightarrow Te_O^X + \frac{1}{2}O_2 \quad (33)$$

The following equation describes the method of calculating solution energy for the reaction 1.

$$E_{Sol} = E\,[S_O^X]_{1\times2\times2} + \frac{1}{2}E\,[O_2] - \frac{1}{8}E\,[S_8] - E[LiPON]_{1\times2\times2} \quad (34)$$

where $E\,[S_O^X]_{1\times2\times2}$ is the total energy of a supercell containing S_O^X defect, $E\,[O_2]$ is the total energy of molecular oxygen and $E\,[S_8]$ is the total energy of bulk S_8. Solution energies are reported in Table 9. The lowest solution energy (3.98 eV) is calculated for S. This is partly due to ionic radius of O^{2-} (1.35 Å) [**39**] being closer to that of S^{2-} (1.84 Å) [**39**] than the other dopants. High endothermic process explains the strong bonding nature of O^{2-} ion with Li^+ ions in the lattice. Solution energies calculated for Se and Te are higher ~2.00 and ~4.00 eV respectively than that calculated for S.

The Li-O and P-O bond distances in the OLi_3P tetrahedral unit is 1.96 Å and 1.56 Å respectively. Clearly there is a significant elongation in the bond lengths (see Figure 9). Bond angles are also expanded with the increasing ionic radius. Such elongation and expansion are reflected in the volume. The Fermi energy gradually increases with increasing ionic radius. The *p* states of the dopants are occupied in the gap without altering the value of the band gap much.

3.5. Incorporation of Lithium

Thermodynamic stability of the LiPON upon Li incorporation upto four Li atoms was assessed by calculating incorporation energies. Structural changes were examined by calculating the volume changes. Electronic structures of the Li-incorporated configurations were analysed by plotting DOSs.

Figure 10 shows the relaxed structures of Li-incorporated configurations. Incorporation energy was calculated using gas phase Li atom and Li metal as reference states. In all cases, incorporation is less favoured with respect to Li metal than gas phase Li atom (see Table 10). This is beacause of the external energy that should be provided to dissociate bulk Li to form Li atoms. The first incorporation is highly positive. The incorporation energy of the system decreases (high postive to less postive or negative) with increasing number of Li^+ ions indicating that the system is themodynamically stable. The formation of single positive charge on the Li was confirmed by the Bader charge analysis. This is due to the stong bonding of Li with lattice oxygen and nitrogen as evidenced by the shorter Li-O (1.84–1.93 Å) and Li-N (2.38 Å) bond distances. Volume gradually increases with the concentration of Li^+ ions.

Calculated total DOS plots of Li-incorporated structures show that there are additional peaks present in the band gap [see Figure 10 (e-h). These peaks belong to Li as evidenced by the atomic DOS plots [see Figure 10 (i-l). The resultant composites are still insulators as their band gaps are relatively large. Our calculations conclude that Li insertion is possible in LiPON retaining its poor electronic conductivity which is one of the requirements for an electrolyte.

4. Conclusion

Using DFT simulations, we examined the defect energetics, solution of dopants and incorporation of lithium in LiPON. We predict that the lowest energy disorder process is the Li_2O Schottky, although this process is highly endothermic, suggesting that the concentration of Li and O vacancies will not be significant at normal temperatures. The results further reveal that the Na, As and S dopants are predicted to be preferentially occupy the Li, P and O sites respectively. Divalent dopant substitution on the Li site is compensated by lithium vacancies. Possible dopant for this process is the Mg that is worth trying experimentally. The doping of Ge on the P site is the favourable process is to create oxygen vacancies and Li interstitials as charge compensating defects. Incorporation of Li atoms (up to four) was considered. Subsequent incorporation expands the volume of the lattice and enhances the stability of Li atoms. Charge analysis confirmed the formation of Li^+ ions in the lattice. Insulating nature of this material is still kept, although there is a slight decrease in the band gap upon each Li incorporation. The current simulation study provides theoretical predictions on dopant engineering strategies and candidate dopants that will be of benefit to experimental optimisation of LiPON electrolyte.

CRediT authorship contribution statement

Navaratnarajah Kuganathan: Conceptualization, Investigation, Formal analysis, Writing - review & editing. Alexander Chroneos: Formal analysis , Writing - review & editing.

Declaration of Competing Interest

The authors declare that there is no competing interest.

Acknowledgement

This research was financially supported by the European Union's H2020 Programme under Grant Agreement no. 824072–HARVESTORE. High Performance Computing Centre at Imperial College London is acknowledged for providing computational facilities and support.

Data Availability Statement

The data that support the findings of this study are available from the corresponding author upon reasonable request.

Supplementary Materials

See the supplementary material for the calculated lattice parameters of bulk materials together with corresponding experimental values and different Li-incorporated configurations.

References

1. C.P. Grey, D.S. Hall, Prospects for lithium-ion batteries and beyond—a 2030 vision, *Nature Communications* 11(1) (2020) 6279.
2. J. Duan, X. Tang, H. Dai, Y. Yang, W. Wu, X. Wei, Y. Huang, Building Safe Lithium-Ion Batteries for Electric Vehicles: A Review, *Electrochemical Energy Reviews* 3(1) (2020) 1-42.
3. Y. Chen, Y. Kang, Y. Zhao, L. Wang, J. Liu, Y. Li, Z. Liang, X. He, X. Li, N. Tavajohi, B. Li, A review of lithium-ion battery safety concerns: The issues, strategies, and testing standards, *Journal of Energy Chemistry* 59 (2021) 83-99.
4. D. Deng, Li-ion batteries: basics, progress, and challenges, *Energy Science & Engineering* 3(5) (2015) 385-418.
5. Y. Zheng, Y. Yao, J. Ou, M. Li, D. Luo, H. Dou, Z. Li, K. Amine, A. Yu, Z. Chen, A review of composite solid-state electrolytes for lithium batteries: fundamentals, key materials and advanced structures, *Chemical Society Reviews* 49(23) (2020) 8790-8839.
6. F. Zheng, M. Kotobuki, S. Song, M.O. Lai, L. Lu, Review on solid electrolytes for all-solid-state lithium-ion batteries, *Journal of Power Sources* 389 (2018) 198-213.
7. M. Weiss, R. Ruess, J. Kasnatscheew, Y. Levartovsky, N.R. Levy, P. Minnmann, L. Stolz, T. Waldmann, M. Wohlfahrt-Mehrens, D. Aurbach, M. Winter, Y. Ein-Eli, J. Janek, Fast Charging of Lithium-Ion Batteries: A Review of Materials Aspects, *Advanced Energy Materials* 11(33) (2021) 2101126.
8. L. Han, M.L. Lehmann, J. Zhu, T. Liu, Z. Zhou, X. Tang, C.-T. Heish, A.P. Sokolov, P. Cao, X.C. Chen, T. Saito, Recent Developments and Challenges in Hybrid Solid Electrolytes for Lithium-Ion Batteries, *Frontiers in Energy Research* 8(202) (2020).
9. G. Yu, Y. Wang, K. Li, D. Chen, L. Qin, H. Xu, J. Chen, W. Zhang, P. Zhang, Z. Sun, Solution-processable Li10GeP2S12 solid electrolyte for a composite electrode in all-solid-state lithium batteries, *Sustainable Energy & Fuels* 5(4) (2021) 1211-1221.
10. H. Yamane, M. Shibata, Y. Shimane, T. Junke, Y. Seino, S. Adams, K. Minami, A. Hayashi, M. Tatsumisago, Crystal structure of a superionic conductor, Li7P3S11, *Solid State Ionics* 178(15) (2007) 1163-1167.
11. J.-P. Han, B. Zhang, L.-Y. Wang, H.-L. Zhu, Y.-X. Qi, L.-W. Yin, H. Li, N. Lun, Y.-J. Bai, Li1.3Al0.3Ti1.7(PO4)3 Behaving as a Fast Ionic Conductor and Bridge to Boost the Electrochemical Performance of Li4Ti5O12, *ACS Sustainable Chemistry & Engineering* 6(6) (2018) 7273-7282.
12. K. Takahashi, K. Hattori, T. Yamazaki, K. Takada, M. Matsuo, S. Orimo, H. Maekawa, H. Takamura, All-solid-state lithium battery with LiBH4 solid electrolyte, *Journal of Power Sources* 226 (2013) 61-64.
13. L. Ye, E. Gil-González, X. Li, Li9.54Si1.74(P1-xSbx)1.44S11.7Cl0.3: A functionally stable sulfide solid electrolyte in air for solid-state batteries, *Electrochemistry Communications* 128 (2021) 107058.
14. M.H. Braga, J.A. Ferreira, V. Stockhausen, J.E. Oliveira, A. El-Azab, Novel Li3ClO based glasses with superionic properties for lithium batteries, *Journal of Materials Chemistry A* 2(15) (2014) 5470-5480.
15. J. Sastre, A. Priebe, M. Döbeli, J. Michler, A.N. Tiwari, Y.E. Romanyuk, Lithium Garnet Li7La3Zr2O12 Electrolyte for All-Solid-State Batteries: Closing the Gap between Bulk and Thin Film Li-Ion Conductivities, *Advanced Materials Interfaces* 7(17) (2020) 2000425.

16. P. López-Aranguren, M. Reynaud, P. Głuchowski, A. Bustinza, M. Galceran, J.M. López del Amo, M. Armand, M. Casas-Cabanas, Crystalline LiPON as a Bulk-Type Solid Electrolyte, *ACS Energy Letters* 6(2) (2021) 445-450.
17. K. Senevirathne, C.S. Day, M.D. Gross, A. Lachgar, N.A.W. Holzwarth, A new crystalline LiPON electrolyte: Synthesis, properties, and electronic structure, *Solid State Ionics* 233 (2013) 95-101.
18. A. Sepúlveda, F. Criscuolo, B. Put, P.M. Vereecken, Effect of high temperature LiPON electrolyte in all solid state batteries, *Solid State Ionics* 337 (2019) 24-32.
19. A. Schwöbel, R. Hausbrand, W. Jaegermann, Interface reactions between LiPON and lithium studied by in-situ X-ray photoemission, *Solid State Ionics* 273 (2015) 51-54.
20. B. Put, Philippe M. Vereecken, A. Stesmans, On the chemistry and electrochemistry of LiPON breakdown, *Journal of Materials Chemistry A* 6(11) (2018) 4848-4859.
21. V. Lacivita, N. Artrith, G. Ceder, Structural and Compositional Factors That Control the Li-Ion Conductivity in LiPON Electrolytes, *Chemistry of Materials* 30(20) (2018) 7077-7090.
22. J.B. Bates, N.J. Dudney, G.R. Gruzalski, R.A. Zuhr, A. Choudhury, C.F. Luck, J.D. Robertson, Electrical properties of amorphous lithium electrolyte thin films, *Solid State Ionics* 53-56 (1992) 647-654.
23. S. Sicolo, K. Albe, First-principles calculations on structure and properties of amorphous Li5P4O8N3 (LiPON), *Journal of Power Sources* 331 (2016) 382-390.
24. P. Henkel, D. Mollenhauer, Uncertainty of exchange-correlation functionals in density functional theory calculations for lithium-based solid electrolytes on the case study of lithium phosphorus oxynitride, *Journal of Computational Chemistry* 42(18) (2021) 1283-1295.
25. G. Kresse, J. Furthmüller, Efficient iterative schemes for ab initio total-energy calculations using a plane-wave basis set, *Physical Review B* 54(16) (1996) 11169-11186.
26. J.P. Perdew, K. Burke, M. Ernzerhof, Generalized Gradient Approximation Made Simple, *Physical Review Letters* 77(18) (1996) 3865-3868.
27. P.E. Blöchl, Projector augmented-wave method, Physical Review B 50(24) (1994) 17953-17979.
28. H.J. Monkhorst, J.D. Pack, Special points for Brillouin-zone integrations, *Physical Review B* 13(12) (1976) 5188-5192.
29. W.H. Press, S.A. Teukolsky, W.T. Vetterling, B.P. Flannery, Numerical recipes in C (2nd ed.): the art of scientific computing, Cambridge University Press1992.
30. S. Grimme, J. Antony, S. Ehrlich, H. Krieg, A consistent and accurate ab initio parametrization of density functional dispersion correction (DFT-D) for the 94 elements H-Pu, *The Journal of Chemical Physics* 132(15) (2010) 154104.
31. G. Henkelman, A. Arnaldsson, H. Jónsson, A fast and robust algorithm for Bader decomposition of charge density, *Computational Materials Science* 36(3) (2006) 354-360.
32. B. Wang, B.C. Chakoumakos, B.C. Sales, B.S. Kwak, J.B. Bates, Synthesis, Crystal Structure, and Ionic Conductivity of a Polycrystalline Lithium Phosphorus Oxynitride with the γ-Li3PO4 Structure, *Journal of Solid State Chemistry* 115(2) (1995) 313-323.
33. G.R. Gardiner, M.S. Islam, Anti-Site Defects and Ion Migration in the LiFe0.5Mn0.5PO4 Mixed-Metal Cathode Material, *Chemistry of Materials* 22(3) (2010) 1242-1248.
34. N. Kuganathan, A. Kordatos, A. Chroneos, Defect Chemistry and Li-ion Diffusion in Li2RuO3, *Scientific Reports* 9(1) (2019) 550.
35. A.R. Armstrong, N. Kuganathan, M.S. Islam, P.G. Bruce, Structure and Lithium Transport Pathways in Li2FeSiO4 Cathodes for Lithium Batteries, *Journal of the American Chemical Society* 133(33) (2011) 13031-13035.
36. F.A. Kröger, H.J. Vink, Relations between the Concentrations of Imperfections in Crystalline Solids, in: F. Seitz, D. Turnbull (Eds.), Solid State Physics, Academic Press1956, pp. 307-435.
37. N. Kuganathan, M.J.D. Rushton, R.W. Grimes, J.A. Kilner, E.I. Gkanas, A. Chroneos, Self-diffusion in garnet-type Li7La3Zr2O12 solid electrolytes, *Scientific Reports* 11(1) (2021) 451.
38. C.S. Johnson, S.H. Kang, J.T. Vaughey, S.V. Pol, M. Balasubramanian, M.M. Thackeray, Li2O Removal from Li5FeO4: A Cathode Precursor for Lithium-Ion Batteries, *Chemistry of Materials* 22(3) (2010) 1263-1270.
39. R. Shannon, Revised effective ionic radii and systematic studies of interatomic distances in halides and chalcogenides, *Acta Crystallographica Section A* 32(5) (1976) 751-767.

Table 1. Calculated and experimental lattice parameters of orthorhombic LiPON.

Parameter	Calculated	Experiment [17]	|Δ| (%)
a (Å)	8.9871	9.0692	0.91
b (Å)	5.3750	5.3999	0.46
c (Å)	4.7129	4.6856	0.58
α=β=γ (°)	90.0	90.0	0.00
V $(Å)^3$	227.66	229.47	0.79

Table 2. Effective Bader charges on each atoms in the relaxed bulk LiPON.

Atom	Bader charge (e)
Li	+1.00
P	+5.00
N	−2.98
O	−1.98, −2.04

Table3. Reaction energies for the formation of LiPON using different chemical reactions.

Reaction	Reaction energy (eV)	Atom economy (%)
$Li_2O + \frac{1}{5} P_2O_5 + \frac{1}{5} P_3N_5 \rightarrow Li_2PO_2N$	−2.66	100
$2\,Li + \frac{1}{4}P_4 + O_2 + \frac{1}{2} N_2 \rightarrow Li_2PO_2N$	−12.22	100
$2\,Li + \frac{1}{4}P_4 + NO_2 \rightarrow Li_2PO_2N$	−12.03	100
$\frac{1}{2}Li_4P_2O_7 + NO \rightarrow Li_2PO_2N + \frac{5}{4}O_2$	2.59	69.5
$Li_2O + \frac{1}{2} P_2O_5 + \frac{1}{2} N_2 \rightarrow Li_2PO_2N + \frac{3}{4}O_2$	0.88	79.1
$Li_3N + LiPO_3 \rightarrow Li_2PO_2N + Li_2O$	−4.22	75.2

Table 4. Intrinsic defect energies calculated for Frenkel, Schottky and anti-site defect processes.

Defect process	Equation number	Reaction energy (eV)/defect
Li Frenkel	8	3.94
P Frenkel	9	10.03
N Frenkel	10	3.98
O Frenkel	11	3.29
Schottky	12	2.98
Li_2O Schottky	13	2.27
P_2O_5 Schottky	14	4.21
Li-P anti-site (isolated)	15	6.80
Li-P anti-site (cluster)	16	4.97

Table 5. Solution energies of alkali dopants (Na, K, Rb and Cs) on the Li site. Volume change with respect to defect-free LiPON is also provided.

Dopant	Ionic radius	Solution energy (eV)/dopant	ΔV/V (%)
Na	0.99	–0.04	0.89
K	1.37	2.14	2.08
Rb	1.52	3.57	2.66
Cs	1.67	6.02	3.45

Table 6. Solution energies of alkali-earth dopants (Mg, Ca, Sr and Ba) on the Li site. The values in the parentheses are the solution energies calculated for M'_{Li}-$Li^{\bullet}_{i}$cluster (M =Mg, Ca, Sr and Ba).

Dopant	Ionic radius	Solution energy (eV)/dopant	Binding energy (eV)/dopant	ΔV/V (%)
Mg	0.71	2.30 (2.08)	–0.22	0.57
Ca	1.00	2.66 (2.26)	–0.40	1.63
Sr	1.18	3.04 (2.46)	–0.58	2.15
Ba	1.35	3.80 (3.06)	–0.74	3.07

Table 7. Solution energies of tetravalent dopants (Si, Ge, Ti, Sn, Zr and Ce) on the P site. The values in the parentheses are the solution energies calculated for defect clusters ($M_P'-Li_i^\bullet$ and $2M_P'-V_O^{\bullet\bullet}$).

Dopant	Ionic radius (Å)	Solution energy (eV)/dopant		Binding energy (eV)/dopant		ΔV/V (%)	
		Charge compensation		Charge compensation		Charge compensation	
		$Li_i^\bullet$	$V_O^{\bullet\bullet}$	$Li_i^\bullet$	$V_O^{\bullet\bullet}$	$Li_i^\bullet$	$V_O^{\bullet\bullet}$
Si	0.26	3.64 (3.28)	4.31 (3.93)	−0.36	−0.38	0.83	1.18
Ge	0.39	5.66 (1.52)	3.98 (2.22)	−4.14	−1.76	1.83	4.26
Ti	0.42	4.46 (4.24)	5.21 (4.61)	−0.22	−0.60	1.70	1.94
Sn	0.55	5.48 (5.24)	6.12 (5.37)	−0.24	−0.75	2.41	3.49
Zr	0.59	6.46 (6.28)	7.10 (6.18)	−0.18	−0.92	2.55	2.75
Ce	0.87	7.90 (7.56)	8.43 (6.69)	−0.34	−1.74	2.94	3.80

Table 8. Solution energies of pnictogen dopants (As, Sb and Bi) on the P site.

Dopant	Ionic radius	Solution energy (eV)/dopant	ΔV/V (%)
As	0.34	0.60	0.73
Sb	0.60	2.68	1.61
Bi	0.76	3.03	2.21

Table 9. Solution energies of chalcogen dopants (S, Se and Te) on the O site.

Dopant	Ionic radius	Solution energy (eV)/dopant	ΔV/V (%)
S	1.84	3.98	1.64
Se	1.98	5.02	2.17
Te	2.21	7.19	3.15

Table 10. Incorporation energies, Bader charges on the incorporated Li atoms and volume change upon successive incorporation.

Reaction	Incorporation energy (eV)/Li		Bader charge (e)	ΔV/V (%)
	Ref: Li atom	Ref: Li bulk		
Li + LiPON → Li.LiPON	1.32	2.99	+1.00	0.92
2Li + LiPON → 2Li.LiPON	0.18	1.85	+1.00 (2)	1.86
3Li + LiPON → 3Li.LiPON	0.06	1.73	+1.00 (3)	3.24
4Li + LiPON → 4Li.LiPON	−0.44	1.23	+1.00 (4)	4.66

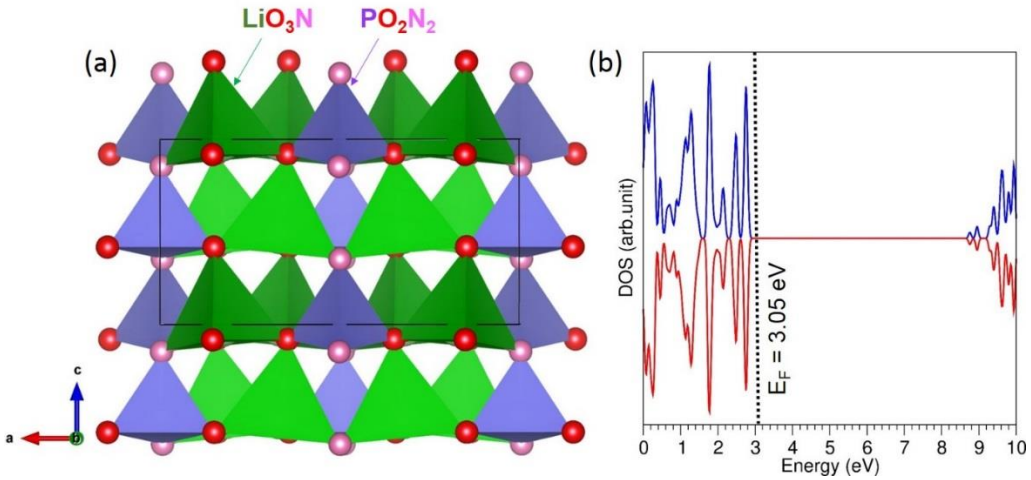

Figure 1. (a) Crystal structure of LiPON and (b) its DOS plot. Vertical dot lines correspond to the Fermi energy level.

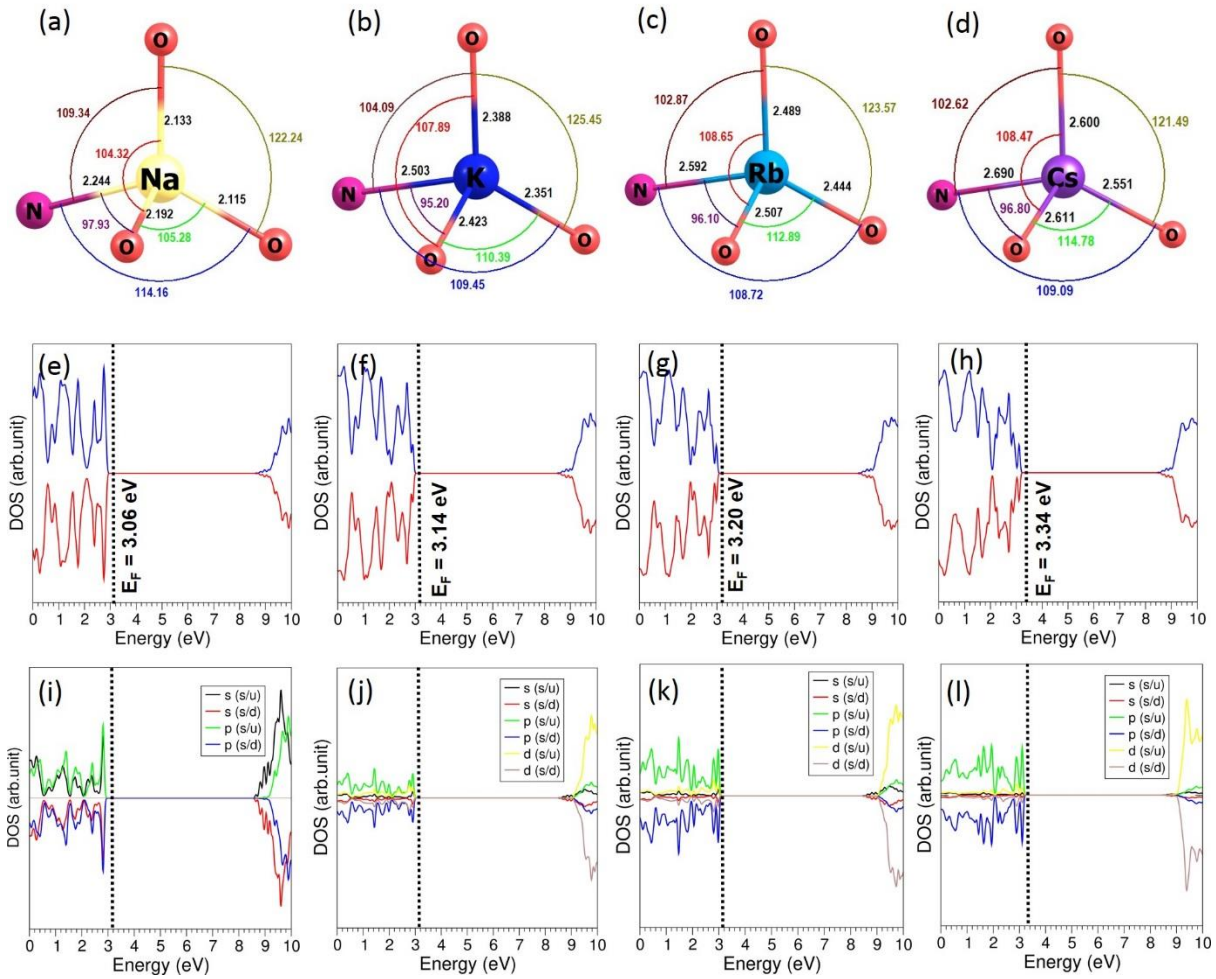

Figure 2. (a-d) Tetrahedral units consisting of each dopants (Na, K, Rb and Cs respectively) on the Li site in the relaxed structures, (e-h) total DOS plots calculated for LiPON doped with Na, K, Rb and Cs respectively and (i-l) corresponding dopant atomic DOS plots.

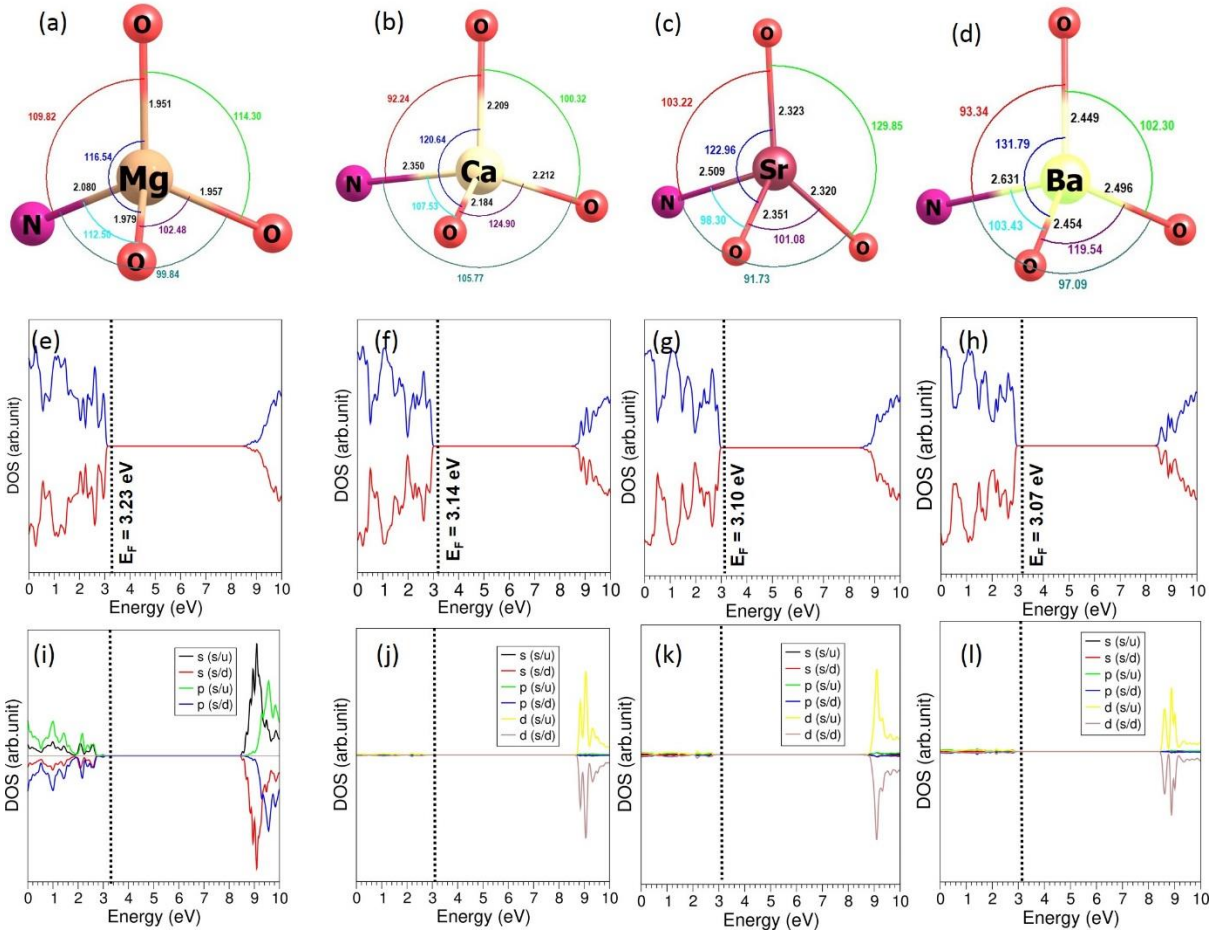

Figure 3. (a-d) Tetrahedral units consisting of each dopants (Mg, Ca, Sr and Ba respectively) on the Li site in the relaxed structures, (e-h) total DOS plots calculated for LiPON doped with Mg, Ca, Sr and Ba respectively and (i-l) corresponding dopant atomic DOS plots.

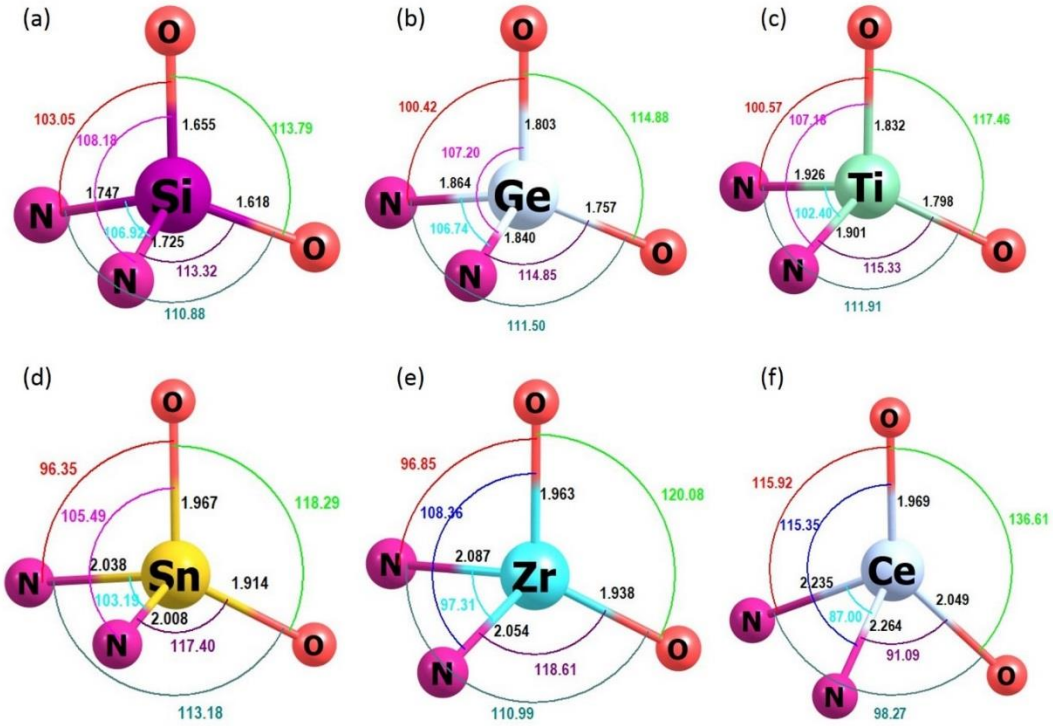

Figure 4. (a-f) Tetrahedral units consisting of each dopants (Si, Ge, Ti, Sn, Zr and Ce respectively) on the P site in the relaxed structures (charge compensation: Li interstitial).

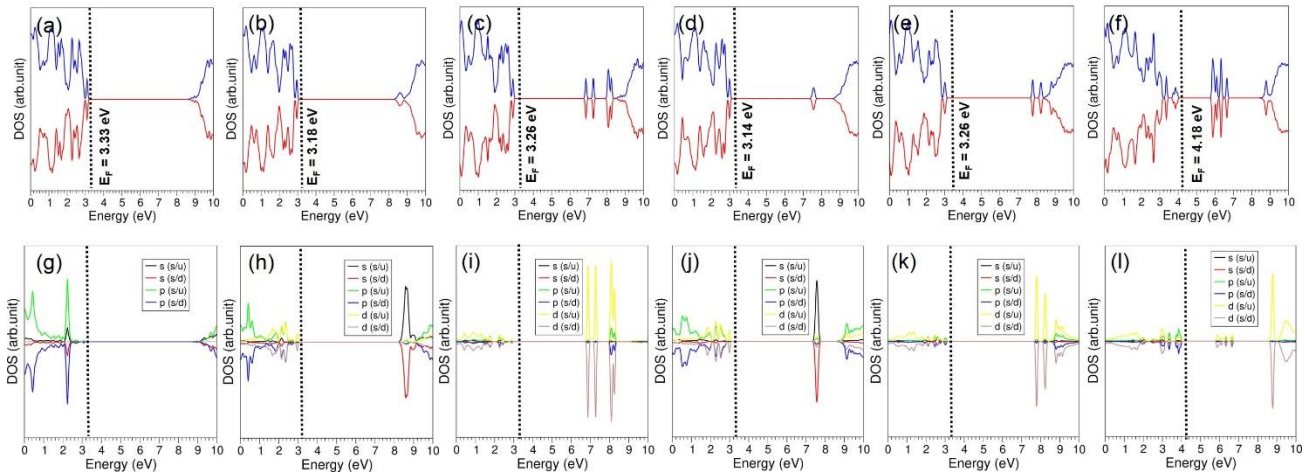

Figure 5. Total DOS plots of (a) Si, (b) Ge, (c) Ti, (d) Sn, (e) Zr and Ce doped on the P site respectively (charge compensation: Li interstitial). Corresponding atomic dopant DOS plots (g-l) are also shown.

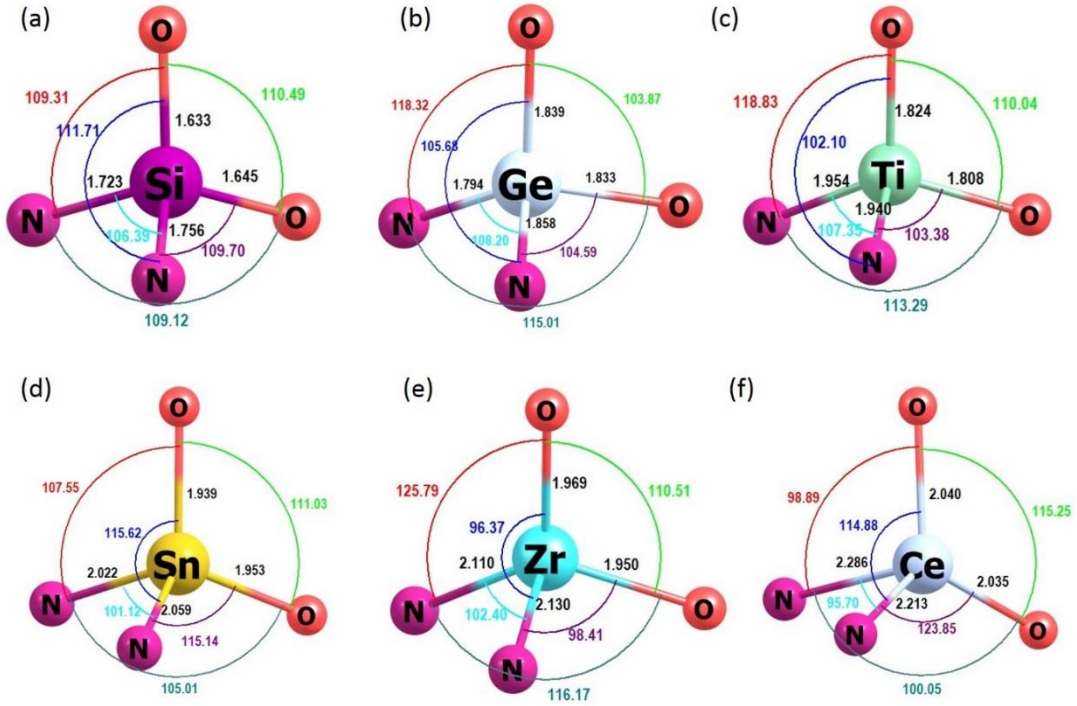

Figure 6. (a-f)Tetrahedral units consisting of each dopants (Si, Ge, Ti, Sn, Zr and Ce respectively) on the P site in the relaxed structures (charge compensation: oxygen vacancy).

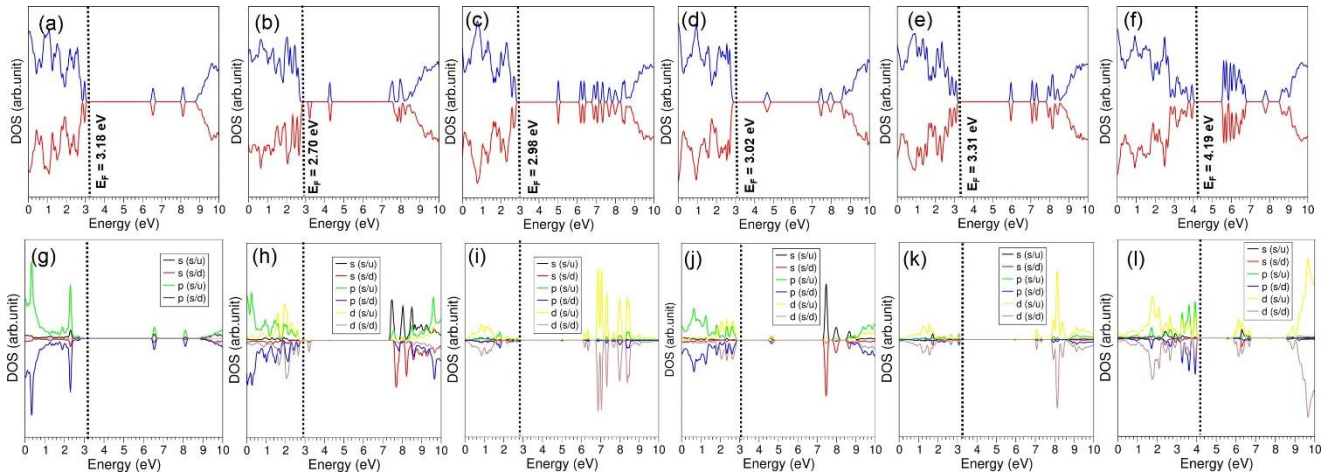

Figure 7. Total DOS plots of (a) Si, (b) Ge, (c) Ti, (d) Sn, (e) Zr and Ce doped on the P site respectively (charge compensation: oxygen vacancy). Corresponding atomic dopant DOS plots (g-l) are also shown.

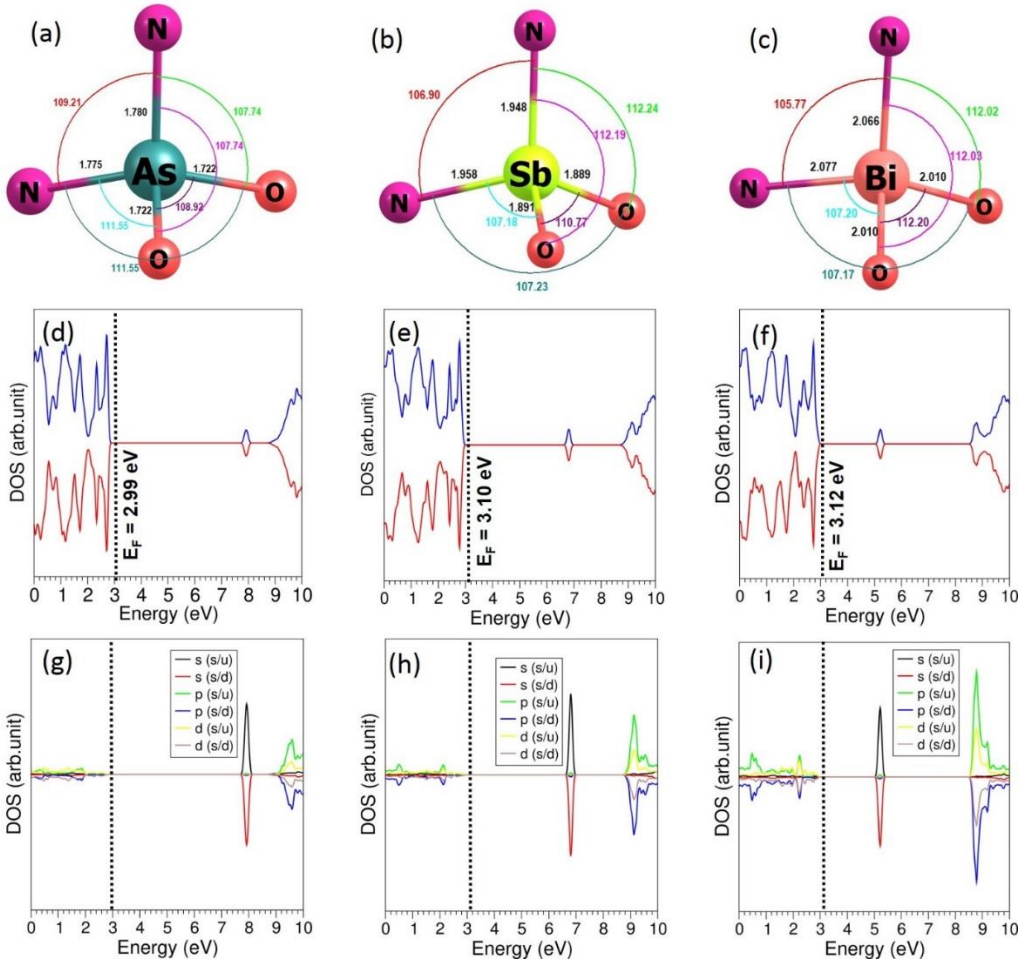

Figure 8. (a-c)Tetrahedral units consisting of each dopants (As, Sb and Bi respectively) on the P site in the relaxed structures, (d-f) total DOS plots calculated for LiPON doped with As, Sb and Bi respectively and (g-i) corresponding dopant atomic DOS plots.

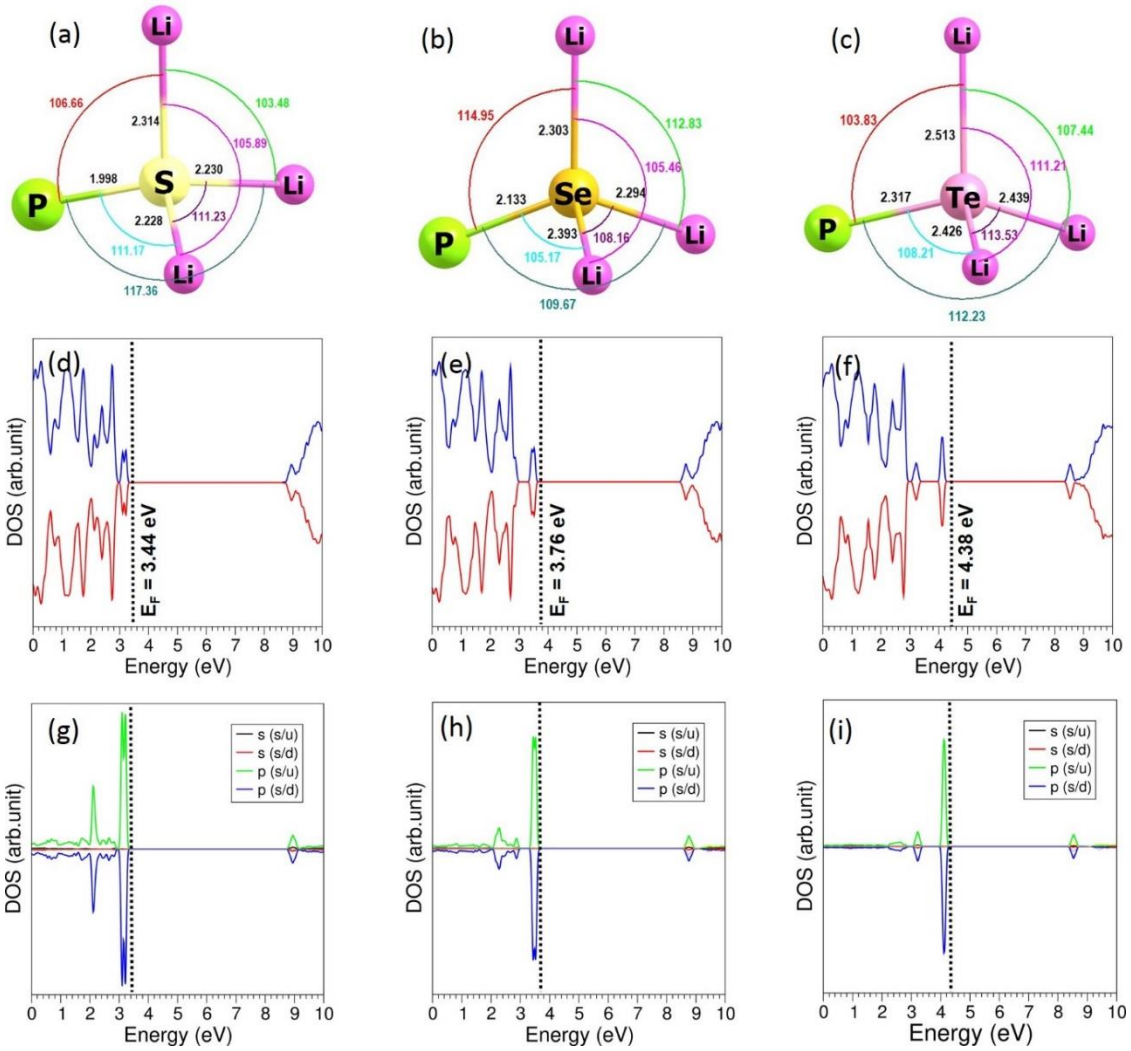

Figure 9. (a-c)Tetrahedral units consisting of each dopants (S, Se and Te respectively) on the O site in the relaxed structures, (d-f) total DOS plots calculated for LiPON doped with S, Se and Te respectively and (g-i) corresponding dopant atomic DOS plots.

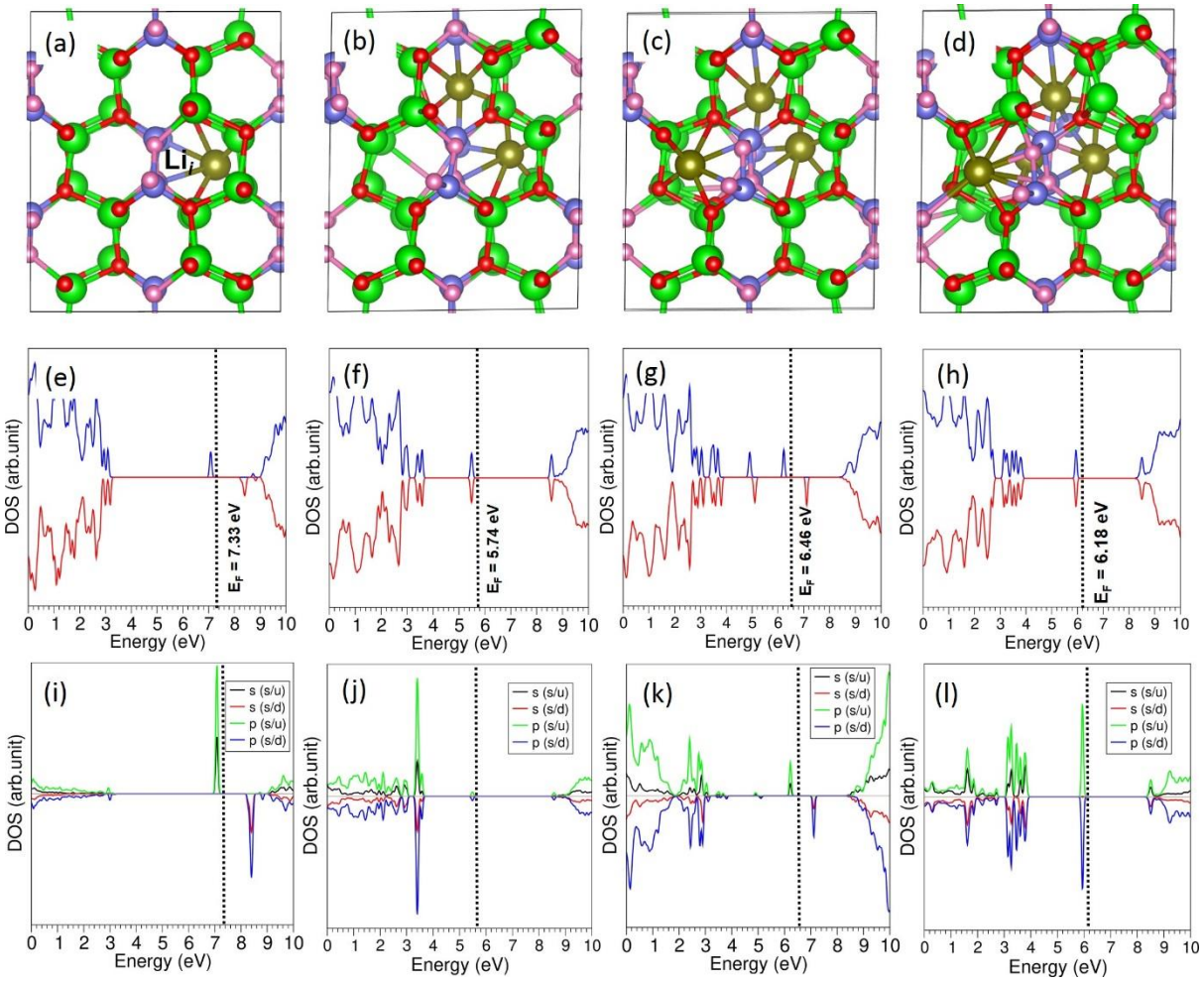

Figure 10. Relaxed structures of (a) a single Li, (b) 2Li, (c) 3Li and (d) 4Li incorporated into LiPON. Corresponding total DOS plots (e-h) and atomic DOS plots of Li (i-l) for each configurations are also shown.